Scripta Materialia 289 (2027) 117681

Contents lists available at ScienceDirect

Scripta Materialia

journal homepage: www.journals.elsevier.com/scripta-materialia

The role of Al on the A2/B2 phase stability in Ti-rich refractory compositionally complex alloys

A. Radi [a], S. Sen [a], V. Tucker [a], C. Tang [b], B. Gorr [b], D. Schliephake [a], M. Heilmaier [a], A. Kauffmann [c,*]

[a] Institute for Applied Materials – Materials Science and Engineering (IAM-WK), Karlsruhe Institute of Technology (KIT), Engelbert-Arnold-Str. 4, 76131 Karlsruhe, Germany
[b] Institute for Applied Materials – Applied Materials Physics (IAM-AMP), Karlsruhe Institute of Technology (KIT), Hermann-von Helmholtz-Platz 1, Karlsruhe, 76344, Baden-Württemberg, Germany
[c] Institute for Materials (IM), Ruhr University Bochum (RUB), Universitätsstr. 150, 44780 Bochum, Germany

ARTICLE INFO

Keywords:
Refractory compositionally complex alloy
High entropy alloys
Microstructure
Decomposition
Ordering

ABSTRACT

The influence of Al content on the microstructural evolution in Ti-rich (50-*x*)Ti-20Mo-15Ta-15Cr-*x*Al (at.%) refractory compositionally complex alloys is revealed. Alloys with $x = 6$, 8, and 10 at.%, designated 6Al, 8Al and 10Al, respectively, were aged at 800 and 1000 °C up to 1000 h and characterized. At 800 °C, increasing Al content promotes the phase separation. While 6Al remains single-phase A2, 8Al develops nanoscale B2 precipitates via nucleation and growth, and 10Al forms interpenetrating A2+B2 presumably via a spinodal decomposition. In the latter cases, B2 is based on Ti(Al,Cr,Mo), while A2 is enriched in Ta and Mo. Differential scanning calorimetry on 10Al indicates that crystallographic ordering precedes phase separation during cooling. At 1000 °C, all alloys remain single-phase A2. Hence, Al governs the critical temperatures of the miscibility gap and ordering, while the ratio of Ta to Ti/(Al,Cr,Mo) dictates the fractions of the constituting phases and the type of phase separation.

A Ti-rich compositionally complex refractory alloy (RCCA) 44Ti-20Mo-15Ta-15Cr-6Al (designated as 6Al, all compositions in at.%) was recently proposed as a novel high-strength structural material, with a density of ~7.5 g/cm^3, being lower than that of typical Ni-base superalloys [1]. 6Al exhibits an almost single-phase microstructure with disordered A2 crystal structure and less than 1 vol.% C15 Laves phase [1]. This alloy plastically deforms in compression at room temperature (RT) and shows oxidation resistance at temperatures up to 1000 °C [1,2]. However, RCCAs that rely solely on solid-solution strengthening possess limited creep resistance, mainly due to the relatively fast diffusion rates inherent to A2 [3–7]. Hence, thermally stable nano- or microscale precipitates are required as barriers impeding dislocation movement [8–10]. Previous research focused on the development of "superalloy-like" microstructures consisting of disordered A2 and ordered B2 [11–21]. While this microstructure is typically achieved at relatively low Ti concentrations, specifically 25–30 at.% [16–20], a new compositional space with the formation of an ordered secondary phase at higher Ti concentrations (40–44 at.%) is introduced while maintaining the lightweight advantage.

Two-phase A2+B2 microstructures in RCCAs can be achieved either by spinodal decomposition [22,23] or nucleation and growth [16], as recently reviewed [24]. Senkov et al. [18] stated that 10Al-20Nb-15Ta-30Ti-5V-20Zr undergoes spinodal decomposition based on the morphological observation of continuous B2 matrix channels surrounding A2 cuboidal precipitates. The verification of the spinodal decomposition was established by Soni et al. [19] and Dasari et al. [25]. Utilizing atom probe tomography (APT), they confirmed the continuous evolution of compositional amplitude and the absence of a nucleation barrier during the early stage of phase separation. Zr acts as the primary driver for this spinodal pathway by forming miscibility gaps with other refractory elements [14,18,19,23]. In contrast, nucleation and growth produces sharp interfaces and distinct chemical partitioning between the phases in the previously studied 27.3Ta-27.3Mo-27.3Ti-8Cr-10Al [16]. Such interfaces are considered essential for controlled microstructure formation during ageing, effective precipitation strengthening under creep conditions, and slow coarsening [11,16]. A2+B2 microstructure formation involves two possible phase transformations: (i) phase separation as outlined above and (ii) crystallographic ordering

* Corresponding author.
E-mail address: alexander.kauffmann@rub.de (A. Kauffmann).

https://doi.org/10.1016/j.scriptamat.2026.117681
Received 31 August 2026; Received in revised form 30 October 2026; Accepted 7 November 2026
Available online 9 November 2026
1359-6462/© 2026 The Authors. Published by Elsevier Inc. on behalf of Acta Materialia Inc. This is an open access article under the CC BY license (http://creativecommons.org/licenses/by/4.0/).
Open access funding enabled and organized by Projekt DEAL.

[17]. During cooling of 27.3Ta-27.3Mo-27.3Ti-8Cr-10Al, phase separation occurs prior to ordering of the minority phase which eventually produces an A2 matrix with B2 precipitates [10,11,17]. Conversely, a higher Al content of 15 at.% triggers ordering before phase separation, causing a phase transition to a (potentially brittle) B2 matrix and subsequent precipitation of the A2 phase. The Al content controls phase separation and sequence of ordering [16,17].

Building on this concept, the present study utilizes Al as a key element to directly address the challenges in introducing the B2 phase into the 6Al reference alloy, while seeking to understand the thermodynamic principle behind its formation. By systematically increasing the Al content, we intentionally promote the formation of B2 to extend the alloy's high-temperature capabilities. We determine how Al concentration shifts (50-*x*)Ti-20Mo-15Ta-15Cr-*x*Al between distinct phase separation mechanisms and alters the resulting topological evolution of the A2+B2 microstructure during long-term exposure at 800 and 1000 °C.

Thermodynamic equilibrium calculations were performed using Pandat with the PanRHEA2025 database (CompuTherm LLC) [26]. Three alloys were synthesized from high-purity elements (>99.9%) via repetitive arc melting (AM/0.5, Edmund Bühler GmbH) under an Ar atmosphere with Zr getter: 44Ti-20Mo-15Ta-15Cr-6Al (6Al), 42Ti-20Mo-15Ta-15Cr-8Al (8Al), and 40Ti-20Mo-15Ta-15Cr-10Al (10Al). After casting, the alloys were homogenized at 1400 °C for 48 h under flowing Ar, establishing the as-homogenized and furnace-cooled (AH) condition. AH samples were subsequently wrapped in Ta and encapsulated in Ar-filled silica tubes. The ampoules were isothermally heat-treated at 800 and 1000 °C for 10, 100, and 1000 h, followed by water-quenching. Samples were metallographically prepared, concluding with polishing using a suspension of 90% colloidal oxide and 10% of 30%-H_2O_2 suspension. Microstructural evolution was analyzed via scanning electron microscope-backscattered electron imaging (SEM-BSE, LEO Gemini 1530, Carl Zeiss), selected area electron diffraction (TEM-SAED, Philips CM 200), and scanning transmission electron microscopy energy-dispersive X-ray spectroscopy (STEM-EDS, Spectra Ultra with Ultra-X detector). Vickers hardness measurements with an applied load of 9.81 N (HV1) were conducted utilizing a Q10A+ hardness tester (Qness). The alloy compositions were verified using inductively coupled plasma optical emission spectrometry (ICP-OES, iCAP 7600 DUO) and carrier gas hot extraction (CGHE, Leco TC600), see Supplementary Table S1. Differential scanning calorimetry (DSC, Netzsch 404 F1 Pegasus) was conducted from room temperature (RT) to 1450 °C at heating rates of 10, 20, and 40 K/min in Ar atmosphere. A sapphire reference was used to obtain dH/dT. The local elemental distributions were quantified by APT. Needle-shaped tips were extracted by focused ion beam (FIB) lift-out from the grain interior in a Helios 5CX dual-beam FIB/SEM (Thermo Fisher Scientific) and shaped by annular milling. APT was performed on a CAMECA LEAP 4000X HR (Cameca Instruments) in laser pulse mode at 50 K, using a 355 nm UV laser (40 pJ, 125 kHz) and 0.5% detection rate. Reconstruction and analysis were executed using Cameca AP Suite 6.3 software.

Thermodynamic equilibrium phase fractions were calculated as a function of temperature to predict the influence of Al concentration on the phase stability (Supplementary Figure S1). An increasing Al content leads to larger B2 phase fractions at 800 °C (7, 14, and 19 at.% in 6Al, 8Al, and 10Al, respectively; Supplementary Figure S1d). No B2 phase formation is anticipated at 1000 °C.

DSC was employed at heating rates of 40 K/min to experimentally investigate the thermal signatures of the phase transformations (Fig. 1). To contextualize the signals, the enthalpy changes of 27.3Ta-27.3Mo-27.3Ti-8Cr-10Al and 25.7Ta-25.6Mo-25.6Ti-8Cr-15Al alloys are included, too [17]. 6Al-AH exhibits no calorimetric evidence of a phase transition. Similarly, 8Al-AH shows no clear calorimetric feature. Conversely, 10Al-AH displays the presence of a mild calorimetric event. In contrast to the weak event in 10Al, the two-phase alloys from literature display pronounced calorimetric peaks corresponding to decomposition and solid-state ordering transition.

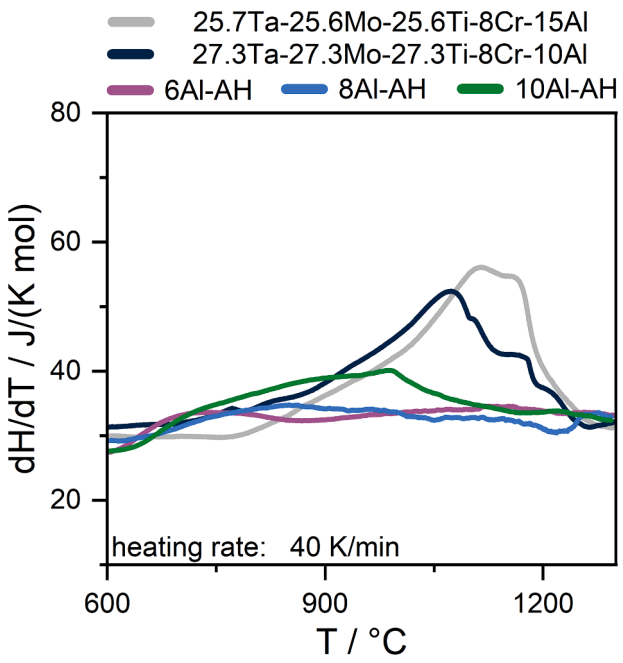


Fig. 1. DSC results for 6Al-AH, 8Al-AH, 10Al-AH in comparison to 25.7Ta-25.6Mo-25.6Ti-8Cr-15Al and 27.3Ta-27.3Mo-27.3Ti-8Cr-10Al [17]. All data obtained at 40 K/min.

Additional DSC experiments were performed on a single 10Al specimen at varying heating rates (Supplementary Figure S2). DSC at 10 K/min clearly reveals two peaks: (i) a broad feature at low temperatures, and (ii) a λ-shaped peak at higher temperatures. In thermal analysis, diffusion-controlled reactions should exhibit a Gaussian-like peak with characteristic temperatures (e.g. onsets) that are heating-rate dependent [27,28]. In case of a 1st order phase transformation, the signal corresponds to the latent heat of transformation. Crystallographic ordering as a continuous phase transition of 2nd order should ideally exhibit λ-shaped anomaly of the heat capacity with a characteristic peak temperature [27]. No latent heat is involved. As ordering is achieved by short-range atomic rearrangements and no long-range diffusion is required, no rate dependence is expected. Indeed, the minimal heating-rate dependence (only 2 K change for 10 to 40 K/min, Supplementary Figure S2) of the peak temperature of the λ-shaped anomaly is consistent with this expectation and might be an artefact from the superposition with the diffusion-controlled reaction. The extrapolation of the peak temperature to 0 K/min yields a transformation temperature of 965 °C. The heat signature of the diffusion-controlled reaction was not further evaluated due to its width and the difficulty defining a proper onset temperature.

The microstructures during ageing at 800 °C were analyzed via SEM-BSE (Fig. 2). 6Al presents a single-phase A2 microstructure even after 1000 h, whereas 8Al and 10Al develop two-phase microstructures. Throughout ageing, 8Al preserves this two-phase microstructure with a bright A2 matrix and a darker-contrast secondary phase. This secondary phase is verified as B2 by TEM-SAED (Fig. 3d–f, a possible Heusler phase is excluded). In contrast, an apparent interpenetrating network of bright- and dark-contrast phases forms in 10Al (Fig. 3c). STEM-EDS analysis of both alloys reveals that Ta and Mo partition to A2, while Ti and Al partition into B2 (Fig. 3a–b). Cr is evenly distributed between the phases. SEM investigations of microstructures annealed at 1000 °C did not reveal any phase transformations (Supplementary Figure S3).

Across all variants and investigated conditions including long-term thermal exposure at 800 and 1000 °C for up to 1000 h (Supplementary Figure S3), Laves phase was occasionally found at grain boundaries. However, quantitative image analysis reveals that it is in all cases remaining strictly below 1 vol.% (Supplementary Figure S4).

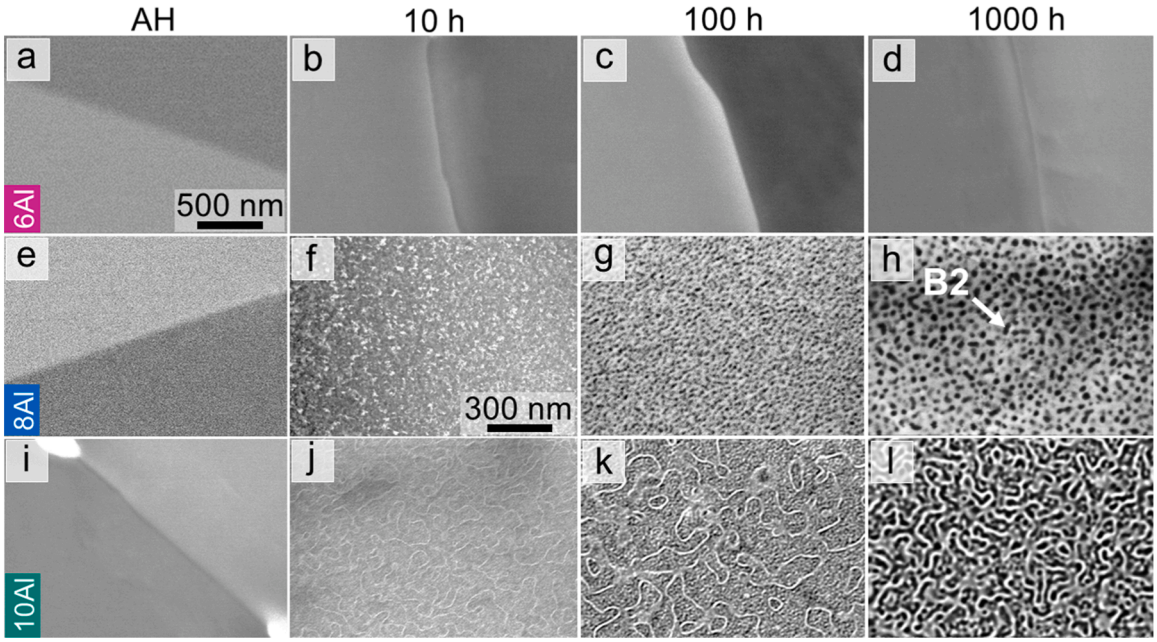


Fig. 2. SEM-BSE micrographs for (a-d) 6Al, (e, g, and h) 8Al, and (i-l) 10Al. Heat treatment conditions as displayed. (f) dark field STEM micrograph for 8Al aged at 800°C/10h; the corresponding TEM-SAED pattern is shown in Fig.3e. Magnifications are as shown in (a) except (f) with a separate scale bar.

Consequently, the Laves phase is considered a negligible constituent and excluded from further analysis.

After 10 h of aging 8Al at 800 °C, the B2 precipitates cannot be resolved by SEM-BSE. Hence, STEM was employed to yield a high density of spherical particles with an average diameter of ~15 nm (bright dots in Fig. 2f). During prolonged exposure, the precipitates coarsen, resulting in an increasing mean precipitate diameter and inter-particle spacing up to (55 ± 5) and (55 ± 10) nm after 1000 h, respectively. The area fraction of the B2 phase remains constant at (21 ± 2) vol.%.

Further increasing the Al content in 10Al not only alters the microstructure into an apparently interpenetrating network of A2+B2 but also significantly increases the B2 area fraction to (49 ± 1) vol.% (Fig. 4a). The coarsening of this A2–B2 network is clearly evidenced. During aging, the mean width of the B2 phase coarsens from (55 ± 15) nm at 10h to (190 ± 55) nm at 1000 h. Instead of the network breaking down into discrete particles, this dimensional growth reflects continuous microstructural coarsening.

The hardness of the alloys (determined by avoiding grain boundaries) depends strongly on the Al content and heat treatment condition (Fig. 4b,c). In the AH state, an increasing hardness with increasing Al content is noted with (450 ± 5), (455 ± 5) and (470 ± 10) HV1 for 6Al, 8Al and 10Al, respectively. During isothermal exposure at 800 °C, the hardness of 6Al remains constant over time, while hardness increases significantly to peak values of (485 ± 5) and (510 ± 5) HV1 in 8Al and 10Al after 10 h, respectively. While a slight decrease is noted for 8Al for longer annealing times at 800 °C, hardness remains essentially stable with further annealing for 10Al. By contrast, the hardness for both 8Al and 10Al remain nearly constant within their overlapping scatter bands at around (460 ± 5) and (475 ± 10) HV1, respectively, up to 1000 h at 1000 °C.

To characterize the elemental partitioning between the coexisting phases, APT was performed on 8Al and 10Al after annealing at 800 °C for 1000 h. Table 1 summarizes the compositions of A2 and B2, together with the composition of the analysed tips. The data confirm the different elemental partitioning of Ta and Mo vs. Ti and Al vs. Cr, as stated above.

A pseudo-ternary, isothermal section for the composition data obtained from APT after 1000 h at 800 °C is shown in Fig. 5a. Ta is chosen as the most potent A2 stabilizing element in one corner. Ti and the sum of the Al, Cr, and Mo contents are taken as the opposite edge. This is due to the experimentally identified ratios of these elements in B2 at 800 °C. $x_{Ti}/(x_{Al}+x_{Cr}+x_{Mo})$ in B2 is 1.05 and 0.97 for 8Al and 10Al, respectively. These particles almost perfectly resemble the stoichiometry of B2 Ti(Al, Cr,Mo). Still, a rather large fraction of Ta is dissolved in B2 contributing to considerable disorder. In a recent simulation study, Zhang et al. [29] revealed the temperature-dependent site occupation in quaternary B2 Mo-Ti-Cr-Al alloys for the first time. According to their evaluation, crystallographic order can be established by different species depending on temperature and composition of the B2 phase. For equimolar MoTiCrAl for instance, a perfect order with Ti and Cr on one sublattice and Mo and Al on the other sublattice is obtained at low temperatures. With increasing temperature, Cr becomes equally distributed among the two lattice sites leaving Ti, Al and Mo with descendent contribution to order. While thermodynamic calculations with the currently available model predict some Mo and Ta content within B2 at 800 °C (see Supplementary Table S2), these two elements do not contribute substantially to order as seen from the site occupations. The trend further continues in the thermodynamic calculations to very low temperature where the ternary B2 Ti(Al,Cr) becomes stable. Thus, the major origin of the discrepancy between thermodynamic calculations and experiments in terms of the temperature- and composition-dependent extent of the miscibility gap is mostly related to the currently not properly considered contribution of Mo to crystallographic order.

At 800 °C, the miscibility gap appears between 6Al and 8Al in Fig. 5a. It further widens with increasing the Al content. The connecting lines between the A2 and B2 represent tie lines of 8Al and 10Al within the miscibility gap. Regarding 8Al, it must be noted that the local chemical composition within the APT specimen slightly deviates from the desired alloy composition of 8Al by +1.8, -0.5, -1.5 at.% in Ti, Ta and (Al+Mo+Cr), respectively. The chosen pseudo-compositional axes in Fig. 5a exacerbate these slight deviations in the representation. Still, the tie line construction of the individual phases and the composition of the entire APT tip match.

Fig. 5b–d illustrate schematic representations of sections parallel to the tie lines obtained within the miscibility gaps. For the 6Al alloy, the hardness was found constant during exposure at 800 and 1000 °C (Fig. 4b,c). This is consistent with the absence of a second phase, confirmed by both SEM-BSE (Fig. 2) and the lack of any thermal

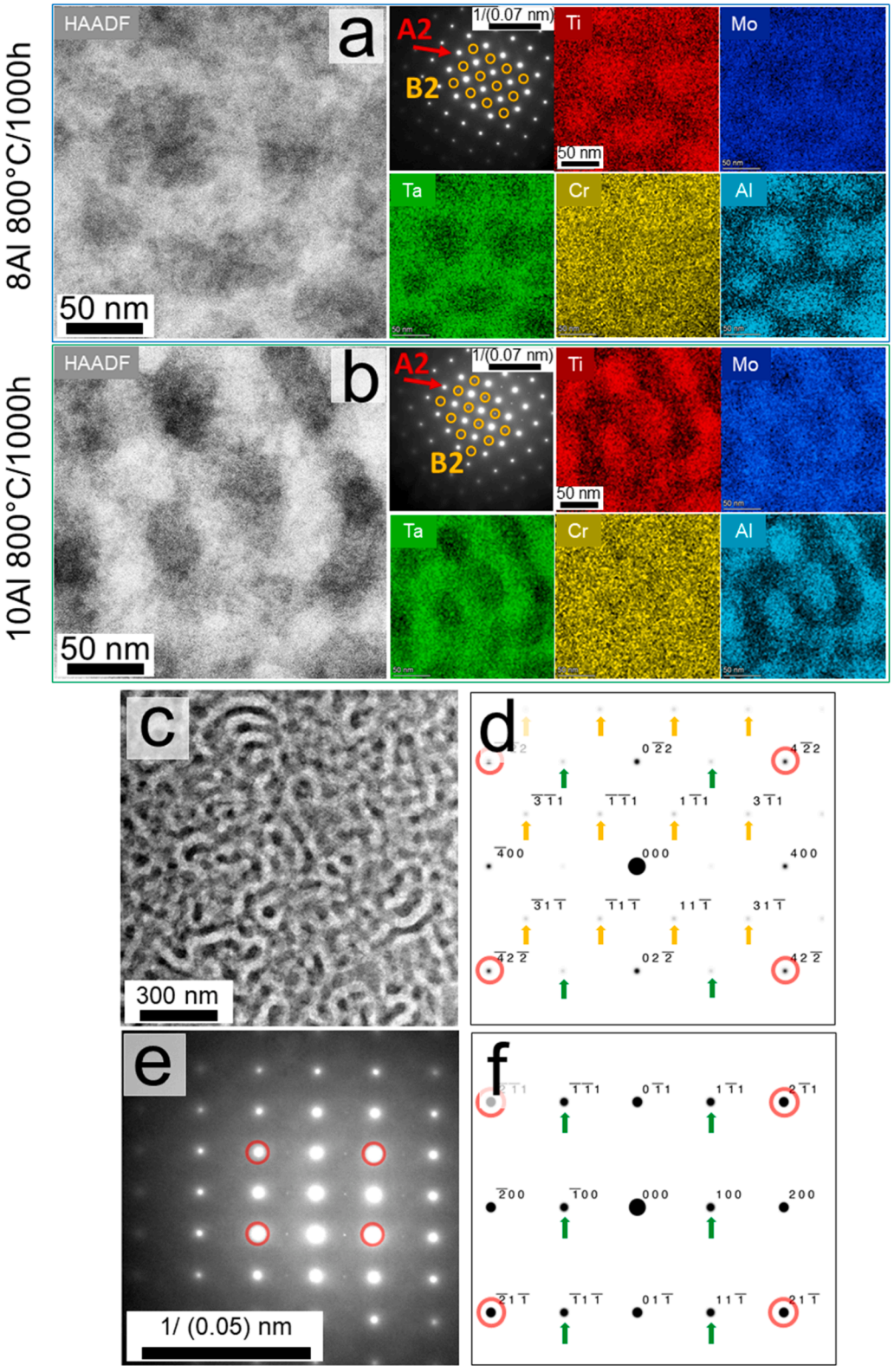


Fig. 3. STEM analysis of (a) 8Al and (b) 10Al, both aged at 800 °C/1000 h. Each panel comprises a HAADF reference image, a TEM-SAED pattern acquired along the [110] zone axis (inset) and STEM-EDS elemental maps for Ti, Mo, Ta, Cr, and Al. In the insets, the red arrow indicates a fundamental A2 spot and the yellow circles indicate B2 superlattice spots. (c) Dark-field STEM micrograph of 10Al aged at 800 °C for 1000 h. TEM-SAED patterns along the [110] zone axis: (d) simulated pattern of the prototypical Heusler ($L2_1$) phase $MnAlCu_2$, indexed with respected to the $L2_1$ unit cell; (e) experimental pattern from 8Al aged at 800 °C/10 h, (f) simulated pattern of the prototypical B2 phase NiAl, indexed with respected to the B2 unit cell. Red circles mark equivalent spots used to align the three patterns, green arrows represent spots common to the B2 and $L2_1$ crystal structure, and yellow arrows represent $L2_1$ unique spots (not seen in (e)).

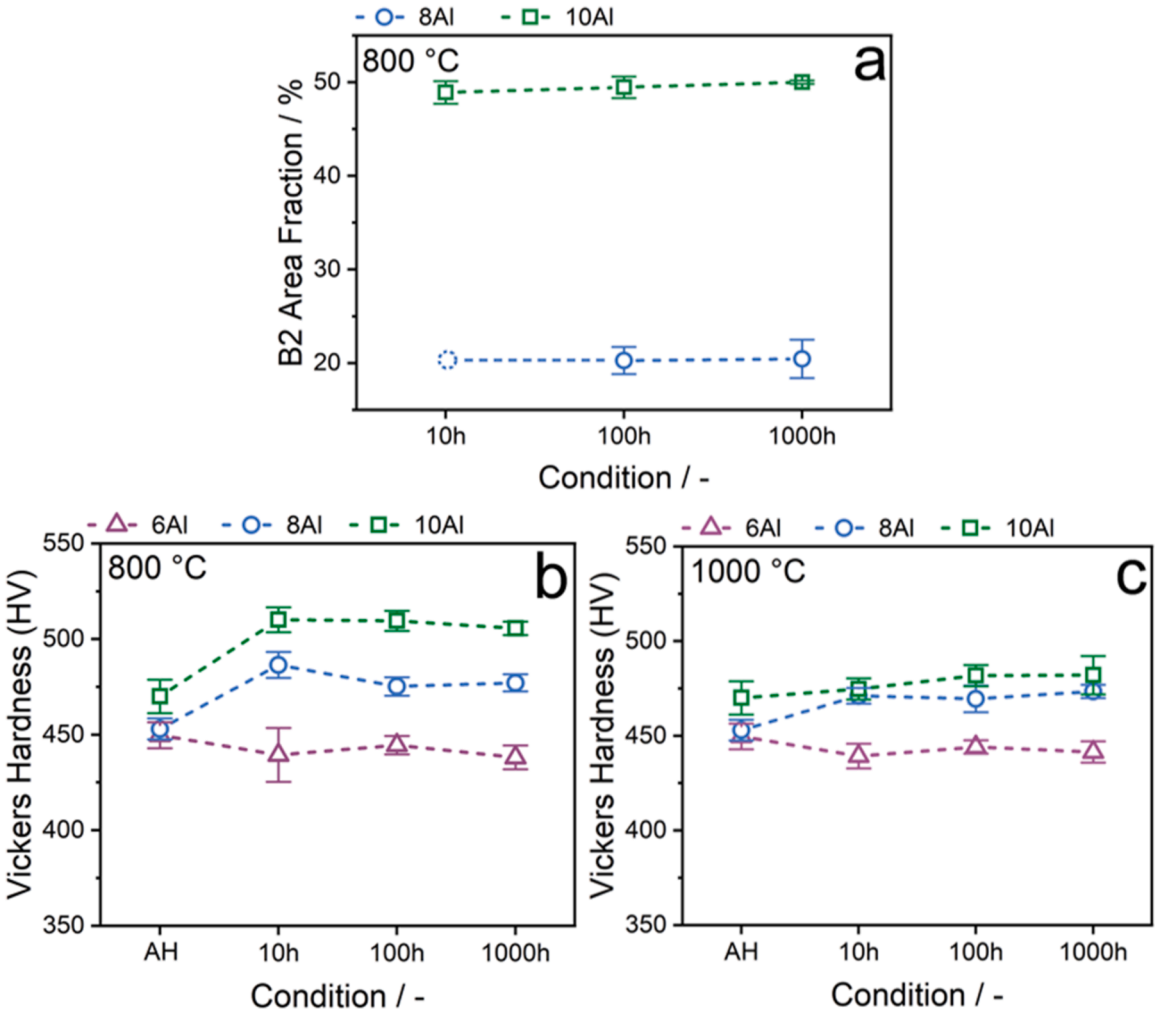


Fig. 4. (a) B2 area fraction in long-term heat-treated conditions of 8Al and 10Al at 800 °C (dashed blue circle is showing the extrapolated B2 area fraction for 8Al at 10h). Hardness of 6Al, 8Al, and 10Al long-term heat treated at b) 800 and c) 1000 °C.

Table 1
Chemical composition obtained via APT (average and uncertainty conservatively rounded to 0.1 at.% precision) for the 8Al and 10Al long-term heat-treated at 800 °C/1000 h: bulk, A2, and B2.

Designation		x_i / at.%				
		Ti	Mo	Ta	Cr	Al
8Al	Bulk	43.8 ± 0.1	19.7 ± 0.1	14.5 ± 0.1	14.1 ± 0.1	7.7 ± 0.1
	A2	43.4 ± 0.1	20.2 ± 0.1	15.2 ± 0.1	14.2 ± 0.1	6.9 ± 0.1
	B2	46.4 ± 0.1	17.3 ± 0.1	10.8 ± 0.1	13.3 ± 0.1	12.0 ± 0.1
10Al	Bulk	40.9 ± 0.1	19.9 ± 0.1	14.6 ± 0.1	14.8 ± 0.1	9.3 ± 0.1
	A2	36.9 ± 0.2	23.3 ± 0.1	19.2 ± 0.1	15.1 ± 0.1	5.3 ± 0.1
	B2	44.9 ± 0.2	16.5 ± 0.1	9.6 ± 0.1	14.4 ± 0.1	14.2 ± 0.1

signature in DSC (Fig. 1). Thus, the miscibility gap demarcated by the binodal line T_{bin} is below 800 °C for this low Al content (Fig. 5b). The distinct tie line direction remains unknown in the present study. No experimental evidence for any ordering was found. Hence, no ordering transition is included.

In contrast, 8Al exhibits a distinct increase in hardness after exposure at 800 °C with a slightly pronounced maximum after 10 h (Fig. 4b) due to the formation of isolated, nanoscale B2 precipitates within A2 and their further coarsening (Fig. 2f–h). During exposure at 1000 °C (Fig. 4c), the hardness remains essentially constant between 10 and 1000 h of annealing. This is consistent with the alloy's location in the A2 single-phase region outside the miscibility gap at 1000 °C (Fig. 5c). Aging at 800 °C leads to presumably nucleation-and-growth-mediated formation of the particles as the alloy composition is located between T_{bin} and the spinodal line T_{spin}. Although B2 is present, no λ-shaped anomaly of the heat capacity associated with solid-state ordering was noticed (Fig. 1). Given that comparable Ti-Mo-Ta-Cr-Al alloys exhibit peaks at similar phase fractions [17], the absence of the signature suggests that the present B2 possesses a lower degree of crystallographic order as the latter determines configurational contribution to the heat capacity [29]. As outlined above, Ta may *not* contribute to order at all and Cr only partitions on one sublattice at low temperatures. Consequently, two scenarios are possible during cooling, (i) ordering takes place after the precipitates have been formed, or (ii) the ordering occurs simultaneously during precipitation. In the latter case, the ordering temperature for the precipitate's compositions must be higher than 800 °C. This scenario is schematically illustrated in Fig. 5c.

By increasing the Al content to 10Al, the alloy composition becomes centered on the tie line at 800 °C (Fig. 5d). A comparably high B2 volume fraction is established which results in a higher hardness compared to 8Al under similar ageing conditions. The constant hardness for increasing annealing times at 800 °C is unexpected when just a

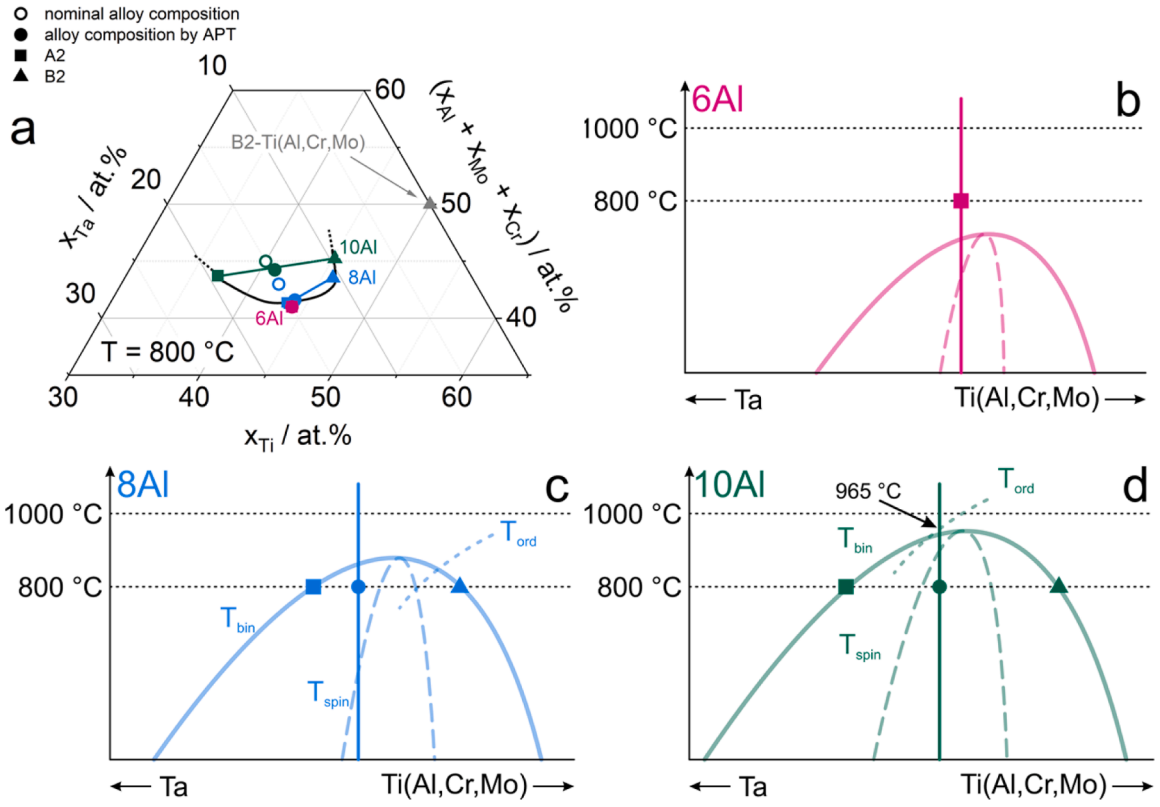


Fig. 5. Semi-quantitative representation of the phase space for the alloys investigated: (a) Pseudo-ternary, isothermal section between Ta-Ti-(Al,Cr,Mo) at 800 °C with compositions from APT included, (b-d) schematic sections along the approximate alloy tie lines illustrating the binodal lines T_{bin} (phase separation), spinodal lines T_{spin} (spinodal decomposition) and ordering temperature T_{ord}.

coarsening of the continuous network of B2 and A2 takes place and the major strengthening contribution results from impediment of dislocation motion within A2 by B2. In this case, a similar decrease as in 8Al would be expected. A scenario where hardness of both phases and their volume fractions account for the hardness of the composite seems unlikely due to the still nanoscopic size of the phase regions after 1000 h of annealing. During spinodal decomposition as might be indicated by the interpenetrating network microstructure, a softening is likely as lattice distortion is usually reduced by the decomposition of the supercooled phase [30]. A factor that remains unknown in this scenario is the development of ordered and disordered regions over time during decomposition. In Ta-free Ti-Mo-Cr-Al alloys, Laube et al. [31] obtained a strength increase of about 300 MPa when establishing order by subtly adjusting the Al content. This may compensate for the hardness drop during decomposition. Yet, the spinodal nature needs to be confirmed and the contribution of order to hardness of the individual phases requires their monolithic synthesis.

In Fig. 5d, the possibility of a spinodal decomposition is assumed and the alloy composition of 10Al is enclosed by the spinodal line T_{spin}. The DSC results indicate the solid-state ordering reaction at 965 °C. During the ordering, antiphase domain boundaries (APDB) form by the coagulation of ordered domains [32,33]. These APDBs can act as nucleation sites for the formation of other phases. A site-specific, heterogeneous formation of a disordered phase was noticed in Ref. [34]. The stripe-like features in Fig. 2j–l are consistent with this. The compositionally distinct A2 phase forms at these sites. During thermal exposure at 1000 °C, the hardness evolutions of 8Al and 10Al are nearly identical (Fig. 4c) because both are in the A2 single-phase region. The slightly higher hardness of 10Al compared to 6Al and 8Al can be rationalized by additional solid solution strengthening due to the higher Al content and the established order in 10Al.

In essence, two important aspects of alloy development within the Ti–Mo–Ta–Cr–Al alloy system are identified in the present work: (i) Al content primarily determines the critical temperature of the miscibility gap and the ordering tendency. (ii) The volume fraction and the type of phase separation are controlled by the ratio of Ta to Ti(Al,Cr,Mo). Ta acts as a potent A2 stabilizing element while the B2 phase originates from partially disordered B2-Ti(Al,Cr,Mo).

CRediT authorship contribution statement

A. Radi: Writing – review & editing, Writing – original draft, Visualization, Project administration, Methodology, Investigation, Formal analysis, Data curation, Conceptualization. **S. Sen:** Writing – review & editing, Formal analysis, Data curation, Conceptualization. **V. Tucker:** Writing – review & editing, Investigation, Formal analysis, Data curation. **C. Tang:** Writing – review & editing, Investigation. **B. Gorr:** Writing – review & editing, Supervision, Resources, Funding acquisition. **D. Schliephake:** Writing – review & editing, Supervision, Methodology, Investigation, Formal analysis, Data curation. **M. Heilmaier:** Writing – review & editing, Writing – original draft, Supervision, Resources, Funding acquisition, Conceptualization. **A. Kauffmann:** Writing – review & editing, Writing – original draft, Visualization, Supervision, Methodology, Funding acquisition, Formal analysis, Data curation.

Declaration of competing interest

The authors declare that they have no known competing financial interests or personal relationships that could have appeared to influence the work reported in this paper.

Acknowledgements

We gratefully acknowledge financial support by the Deutsche

Forschungsgemeinschaft (DFG) with in the project 524725651 (KA 4631/6-1, HE 1872/45-1, and GO 2283/8-1). We acknowledge the chemical analysis by HCGE at the Institute for Applied Materials (IAM-AWP) by Dr. Bergfeldt, Karlsruhe Institute of Technology (KIT). We express our gratitude to Dr. Carsten Schroer for his fruitful contribution to this work.

Supplementary materials

Supplementary material associated with this article can be found, in the online version, at doi:10.1016/j.scriptamat.2026.117681.

Data availability

The data presented in this study are available in Zenodo at https://doi.org/10.5281/zenodo.21770333 under CC BY-SA 4.0 license. Further information is available upon request with alexander.kauffmann@rub.de.

References

[1] A. Radi, D. Schliephake, S. Sen, R.J. Vikram, S. Dixit, J.L. Riedel, L. Yang, C. Tang, B. Gorr, A. Kauffmann, M. Heilmaier, Design of lightweight high-temperature structural materials based on Ti-Mo-Ta-Cr-Al refractory compositionally complex alloys, Part I: Phase stability and mechanical properties, J. Alloys Metall. Syst. 12 (2025) 100219, https://doi.org/10.1016/j.jalmes.2025.100219.

[2] C. Tang, A. Radi, M. Dürrschnabel, U. Jäntsch, M. Klimenkov, A. Kauffmann, M. Heilmaier, C. Schroer, B. Gorr, Design of lightweight high temperature structural materials based on Ti–Mo–Ta–Cr–Al refractory compositionally complex alloys, Part II: High temperature oxidation behavior, J. Alloys Metall. Syst. 12 (2025) 100217, https://doi.org/10.1016/j.jalmes.2025.100217.

[3] T. Yu, L. Qi, S. Ramprakash, Y. Wang, Computational studies on BCC superalloys, Scr. Mater. 267 (2025) 116804, https://doi.org/10.1016/j.scriptamat.2025.116804.

[4] Q. He, X. Wang, Q. Wang, H. Wang, R. Ding, Z. Chen, R. Sun, G. Mi, J. Gu, Y. Yang, Designing refractory complex concentrated alloys for extreme environments, Curr. Opin. Solid State Mater. Sci. 41 (2026) 101255, https://doi.org/10.1016/j.cossms.2026.101255.

[5] O.N. Senkov, S. Gorsse, D.B. Miracle, High temperature strength of refractory complex concentrated alloys, Acta Mater 175 (2019) 394–405, https://doi.org/10.1016/j.actamat.2019.06.032.

[6] W.J. Carpenter, E.P. George, Perspectives on refractory high-entropy alloys, J. Mater. Res. 40 (2025) 1887–1901, https://doi.org/10.1557/s43578-025-01630-7.

[7] D.B. Miracle, O.N. Senkov, C. Frey, S. Rao, T.M. Pollock, Strength vs temperature for refractory complex concentrated alloys (RCCAs): a critical comparison with refractory BCC elements and dilute alloys, Acta Mater 266 (2024) 119692, https://doi.org/10.1016/j.actamat.2024.119692.

[8] O.N. Senkov, D.B. Miracle, K.J. Chaput, J.P. Couzinie, Development and exploration of refractory high entropy alloys - a review, J. Mater. Res. 33 (2018) 3092–3128, https://doi.org/10.1557/jmr.2018.153.

[9] W. Xia, X. Zhao, L. Yue, Z. Zhang, A review of composition evolution in Ni-based single crystal superalloys, J. Mater. Sci. Technol. 44 (2020) 76–95, https://doi.org/10.1016/j.jmst.2020.01.026.

[10] L. Yang, A. Pramanik, S. Sen, S. Dixit, M. Muench, R.J. Vikram, D. Schliephake, Y. M. Eggeler, A. Chauhan, M. Heilmaier, A. Kauffmann, Creep-induced microstructural evolution in an A2-B2 superalloy, Adv. Eng. Mater. 28 (2026) e202503180, https://doi.org/10.1002/adem.202503180.

[11] L. Yang, S. Sen, D. Schliephake, R.J. Vikram, S. Laube, A. Pramanik, A. Chauhan, S. Neumeier, M. Heilmaier, A. Kauffmann, Creep behavior of a precipitation-strengthened A2-B2 refractory high entropy alloy, Acta Mater 288 (2025) 120827, https://doi.org/10.1016/j.actamat.2025.120827.

[12] D.B. Miracle, O.N. Senkov, A critical review of high entropy alloys and related concepts, Acta Mater 122 (2017) 448–511, https://doi.org/10.1016/j.actamat.2016.08.081.

[13] D.B. Miracle, M.H. Tsai, O.N. Senkov, V. Soni, R. Banerjee, Refractory high entropy superalloys (RSAs), Scr. Mater 187 (2020) 445–452, https://doi.org/10.1016/j.scriptamat.2020.06.048.

[14] O.N. Senkov, J.K. Jensen, A.L. Pilchak, D.B. Miracle, H.L. Fraser, Compositional variation effects on the microstructure and properties of a refractory high-entropy superalloy AlMo0.5NbTa0.5TiZr, Mater. Des. 139 (2018) 498–511, https://doi.org/10.1016/j.matdes.2017.11.033.

[15] D.B. Miracle, M.H. Tsai, O.N. Senkov, V. Soni, R. Banerjee, Refractory high entropy superalloys (RSAs), Scr. Mater 187 (2020) 445–452, https://doi.org/10.1016/j.scriptamat.2020.06.048.

[16] S. Laube, A. Kauffmann, S. Schellert, S. Seils, A.S. Tirunilai, C. Greiner, Y. M. Eggeler, B. Gorr, H.J. Christ, M. Heilmaier, Formation and thermal stability of two-phase microstructures in Al-containing refractory compositionally complex alloys, Sci. Technol. Adv. Mater. 23 (2022) 692–706, https://doi.org/10.1080/14686996.2022.2132118.

[17] S. Laube, S. Schellert, A. Srinivasan Tirunilai, D. Schliephake, B. Gorr, H.J. Christ, A. Kauffmann, M. Heilmaier, Microstructure tailoring of Al-containing compositionally complex alloys by controlling the sequence of precipitation and ordering, Acta Mater. 218 (2021) 117217, https://doi.org/10.1016/j.actamat.2021.117217.

[18] O.N. Senkov, S.A. Kube, J.W. Drazin, V. Soni, D.B. Miracle, T.M. Butler, T. M. Pollock, R. Banerjee, Thermal and elastic properties of an A2/B2 refractory high entropy superalloy and its constituent phases, Met. Mater. Trans. Phys. Met. Mater. Sci. 55 (2024) 2704–2717, https://doi.org/10.1007/s11661-024-07429-1.

[19] V. Soni, B. Gwalani, T. Alam, S. Dasari, Y. Zheng, O.N. Senkov, D. Miracle, R. Banerjee, Phase inversion in a two-phase, BCC+B2, refractory high entropy alloy, Acta Mater 185 (2020) 89–97, https://doi.org/10.1016/j.actamat.2019.12.004.

[20] V. Soni, O.N. Senkov, J.P. Couzinie, Y. Zheng, B. Gwalani, R. Banerjee, Phase stability and microstructure evolution in a ductile refractory high entropy alloy Al10Nb15Ta5Ti30Zr40, Mater. (Oxf) 9 (2020) 100569, https://doi.org/10.1016/j.mtla.2019.100569.

[21] E.A. Lass, On the Thermodynamics and Phase Transformation Pathways in BCC-B2 Refractory Compositionally Complex Superalloys, Metall. Mater. Trans. A Phys. Metall. Mater. Sci. 53 (2022) 4481–4498, https://doi.org/10.1007/s11661-022-06844-6.

[22] S. Dasari, V. Soni, A. Sharma, O.N. Senkov, D.B. Miracle, H.L. Fraser, Y. Wang, R. Banerjee, Concomitant clustering and ordering leading to B2 + BCC microstructures in refractory high entropy alloys, Trans. Indian Inst. Met. 75 (2022) 907–916, https://doi.org/10.1007/s12666-021-02518-w.

[23] T.E. Whitfield, E.J. Pickering, L.R. Owen, C.N. Jones, H.J. Stone, N.G. Jones, The effect of Al on the formation and stability of a BCC – B2 microstructure in a refractory metal high entropy superalloy system, Materialia (Oxf). 13 (2020) 100858. 10.1016/j.mtla.2020.100858.

[24] V. Soni, Y. Wang, J.P. Couzinié, H.L. Fraser, R. Banerjee, Phase transformation pathways in BCC-B2 superalloys, Scr. Mater. 267 (2025), https://doi.org/10.1016/j.scriptamat.2025.116734.

[25] S. Dasari, A. Sharma, V. Soni, Z. Kloenne, H. Fraser, R. Banerjee, Crystallographic and compositional evolution of ordered B2 and disordered BCC phases during isothermal annealing of refractory high-entropy alloys, Microsc. Microanal. 29 (2023) 303–313, https://doi.org/10.1017/S1431927622012053.

[26] Pandat 2025 database manual PanRHEA Database for multi-component refractory high entropy alloys (RHEA), 2025. https://doi.org/https://computherm.com/docs.

[27] F. Stein, M. Palm, Re-determination of transition temperatures in the Fe–Al system by differential thermal analysis, Int. J. Mater. Res. 98 (2007) 580–588, https://doi.org/10.3139/146.101512.

[28] H.K. Cammenga, W. Eysel, E. Gmelin, W. Hemminger, V. Krlmer, The temperature calibration of scanning calorimeters purpose and scope of application of the recommendation, Thermochim. Acta 160 (1990) 1–12.

[29] J. Zhang, K. Lechner, M. Maßwohl, P. Spoerk-Erdely, D. Holec, Study of ordering in (MoCrTi)100-xAlx refractory high-entropy alloys using machine learning interatomic potential, J. Mater. Res. Technol. 45 (2026) 918–929, https://doi.org/10.1016/j.jmrt.2026.09.075.

[30] S. Drescher, S. Seils, D. Pohl, B. Rellinghaus, A. Kauffmann, M. Heilmaier, J. Freudenberger, Softening by spinodal decomposition in Au–Cu–Ni–Pd–Pt high-entropy alloys, Mater. Sci. Eng.: A 887 (2023), https://doi.org/10.1016/j.msea.2023.145772.

[31] S. Laube, G. Winkens, A. Kauffmann, J. Li, C. Kirchlechner, M. Heilmaier, Strength of disordered and ordered Al-containing refractory high-entropy alloys, Adv. Eng. Mater. 26 (2024) 2301797, https://doi.org/10.1002/adem.202301797.

[32] S.M. Allen, J.W. Cahn, Mechanisms of phase transformations within the miscibility gap of Fe-rich Fe-Al alloys, Acta Metall. 24 (1976) 425–437, https://doi.org/10.1016/0001-6160(76)90063-8.

[33] M.J. Marcinkowski, N. Brown, Direct observation of antiphase boundaries in the Fe3Al superlattice, J. Appl. Phys. 33 (1962) 537–552, https://doi.org/10.1063/1.1702463.

[34] H. Chen, A. Kauffmann, S. Seils, T. Boll, C.H. Liebscher, I. Harding, K.S. Kumar, D. V. Szabó, S. Schlabach, S. Kauffmann-Weiss, F. Müller, B. Gorr, H.J. Christ, M. Heilmaier, Crystallographic ordering in a series of Al-containing refractory high entropy alloys Ta–Nb–Mo–Cr–Ti–Al, Acta Mater. 176 (2019) 123–133, https://doi.org/10.1016/j.actamat.2019.07.001.